Synthesis of Holey Graphene Nanoparticle Compounds

David L. White,[†] *Levi Lystrom,*[‡] *Xiaoyun He,*[†] *Seth C. Burkert,*[†] *Dmitri S. Kilin,*[‡] *Svetlana Kilina,*[‡] *and Alexander Star*[†,§,]*

[†]Department of Chemistry, University of Pittsburgh, Pittsburgh, Pennsylvania, 15260, USA

[‡]Department of Chemistry and Biochemistry, North Dakota State University, Fargo, North Dakota, 58102, USA

[§]Department of Bioengineering, University of Pittsburgh, Pittsburgh, Pennsylvania 15261, USA

Keywords: Covalent organic frameworks, DFT, metal nanoparticle composites, HOPG, reactive ion etching

Abstract:

Bulk scale syntheses of sp^2 nanocarbon have typically been generated by extensive chemical oxidation to yield graphite oxide from graphite followed by a reductive step. Materials generated via harsh random processes lose desirable physical characteristics. Loss of sp^2 conjugation inhibits long range electronic transport and the potential for electronic band manipulation. Here we present a nanopatterned holey graphene (HG) material electronically hybridized with metal containing nanoparticles. Oxidative plasma etching of highly ordered pyrolytic graphite (HOPG) via previously developed COF-5 templated patterning yields bulk scale material for electrocatalytic applications and fundamental investigations into band structure engineering of nanocomposites. We establish broad ability (Ag, Au, Cu, and Ni) to grow metal containing nanoparticles in patterned holes in a metal precursor dependent manner without reducing agent. Graphene nanoparticle compounds (GNCs) show metal contingent changes in valence band structure. Density functional theory (DFT) investigations reveal preferences for uncharged metal states, metal contributions to the valence band, and embedding of nanoparticles over surface incorporation. Ni-GNCs show activity for oxygen evolution reaction (OER) in alkaline media (1 M KOH). Electrocatalytic activity exceeds 10,000 mA/mg of Ni, stability for two hours of continuous operation, and is kinetically consistent via Tafel slope with $Ni(OH)_2$ based catalysis.

Introduction:

Graphene's intensive research effort has been justified in the numerous results generated for a variety of potential applications.[1-9] Many prominent results have been in the unique electronic properties of the layers of sp^2 carbon and their potential as electrocatalytic supports and materials.[10-18] While the incorporation of graphene oxide and reduced graphene oxide into composites with a variety of heteroatom doping has received substantial attention,[19-21] less consideration has been directed at the possibilities of materials which retain sp^2 conjugation. So-called holey graphene materials have been synthesized in a variety of routes but most commonly through the further oxidation of graphene oxide materials.[22-28] These materials have already lost sp^2 conjugation through the initial oxidation process and therefore lack some of the crucial electronic properties needed for use in functional materials. To generate the milligram scale of material needed for electrocatalytic applications while also retaining sp^2 conjugation, we have developed a synthetic procedure for the generation of high-density holes in highly ordered pyrolytic graphite (HOPG) and exfoliation of these materials into aqueous environments.

Here we present a scalable technique for the generation of holey graphene (HG) (average of 38% mass exfoliated from a given flake n = 27) derived from HOPG (Scheme 1). HG is synthesized by solvothermal growth of a covalent organic framework (COF) template onto HOPG flakes followed by reactive ion etching (RIE). Production of HG by this method has several distinct advantages over current synthetic techniques. Relatively large sheets measuring micrometers in diameter are densely decorated with few nanometer sized holes imprinted from the patterned COF. Both metal nanoparticles and metal containing nanoparticles can be grown into the holes at room temperature without the use of additional reducing agents. The hypothesized mechanism for this growth is the intact conjugated sp^2 network donating electrons to facilitate reduction of the metal ions forming nanoparticles in addition to further oxidation of the holey graphene edge moieties. The patterned holes of the HG act as confining sites restricting the overall size of the nanoparticles preventing nanoparticle aggregation. The nanoparticles are held in place by the underlying HG even under the presence of high-energy electron beams (200 KeV). Spherical size-limited nanoparticle growth is dictated by the relative ratio of metal salt precursor to HG.

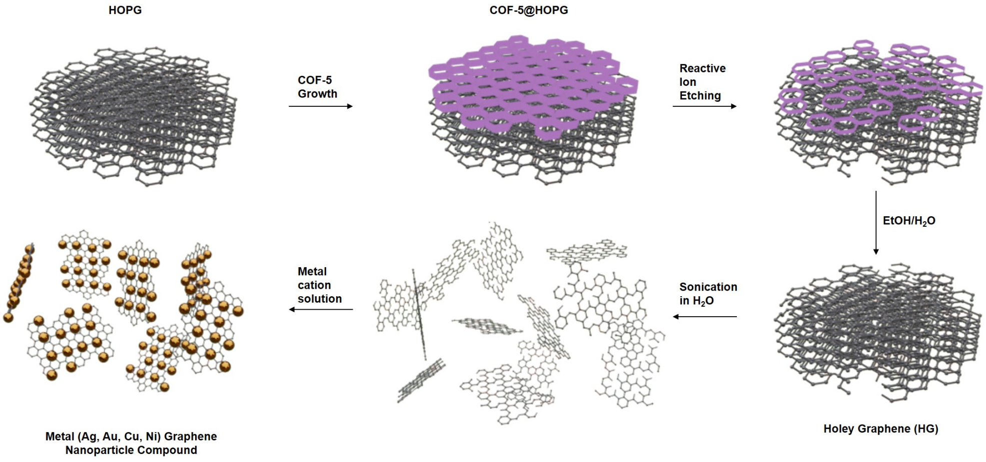

Scheme 1: Synthesis of holey graphene (HG) from HOPG and deposition of metal nanoparticles inside holes to yield graphene nanoparticle compounds (GNCs).

Results and Discussion:

For the process of RIE-COF-5 patterning tight control over both the COF growth and RIE conditions must be considered.[29] If the ratio of hexahydroxytriphenylene to phenylbisboronic acid (HHTP:PBBA) falls outside of the precise ratio (1:3 molar ratio), the patterning is inconsistent leading to under patterning or over patterning if the HHTP is too high or too low respectively (Figure S1). Additionally, a wide range of RIE conditions were explored (Figure S2). Previously in the case of single layer graphene, we optimized hole formation based on the electronic properties (current on/off ratio) of field-effect transistor (FET) devices.[30] Here we optimize RIE conditions based on both perceived discrete hole formation in SEM as well as Raman characteristics like formation of D' peak (1610 cm^{-1}) and relatively small D (1350 cm^{-1}) to G (1500 cm^{-1}) ratios (Figure S3).[31] Another consideration here is the formation of relatively deep holes inside HOPG to maximize material generated. RIE conditions can be challenging to optimize due to the relatively thin layer of COF-5 present (<100 nm), as observed in our previous investigation into single layer graphene,[27] which can be entirely removed in over-etching conditions. Optimization was initially performed with respect to RIE pressure and power while holding time constant. After identifying desired morphological characteristics from the pressure and power conditions, time was optimized to yield deepest patterning to maximize the production of material. The goal of the optimization was to optimize contiguous flake size while achieving dense and deep patterning of holey features. While two primary conditions emerged as viable, only 200 mTorr with 100 W for 30 seconds was selected for further study to limit redundancy.

The finalized condition and the patterning yielded can be seen via SEM (Figure 1a). Dense features are present across large areas of HOPG flake and contiguous flakes that are larger than one micrometer in diameter can be identified. Exfoliation into pure water can yield substantial amount of material that are synthesis-dependent. After three hours of sonication, as little at 0.1 mg/mL can go into solution and as much as 1 mg/mL can be present for the same RIE conditions. TEM observations of ten times diluted solutions can be used to evaluate the retention of patterning after exfoliation (Figure 1b). Large flakes can still be identified in the TEM images with dense patterning of nanometer sized features (4.30 nm ± 1.52 nm, n = 83). After stirring with an optimized concentration of metal salt solution for one-hour, numerous nanoparticles can be identified (Figure 1c). The formed nanoparticles have a relatively small size distribution (2.86 nm ± 0.66 nm, n = 43) with particle size that matches the COF hole pattern (2.7 nm) well. We expect a range of different hole pattern sizes due to the nature of the RIE patterning. Patterning in general does not yield a completely anisotropic etch profile leading to conical type etching into the HOPG flake. Therefore, HG in solution should retain material that is ranging in hole distributions which can explain the discrepancy between the material before and after nanoparticle reduction (Figure 1b and 1c).

AFM imaging of the patterned flakes after washing the residual COF from RIE reveal correspondence between SEM and AFM imaging (Figure 1d). While the holes show minor height differences as compared to the top of the flake the trenches formed show more than 30 nm of height difference. This indicates patterning is potentially reaching as deep as 100 layers into the HOPG, assuming 0.33 nm interlayer spacing. The primary reason that AFM imaging does not reveal more depth for the top features is the relatively small horizonal features which inhibit the tip from probing the deep features. Trenches could be viewed as non-ideal patterning, but the density of the trenches still leaves micrometer-sized flakes that are retained after exfoliation. AFM images of exfoliated sheets reveal large sheets with a wider distribution of holes then the as-patterned HOPG but still demonstrating single layer thickness (Figure 1e). Single sheets are observed here (Figures 1b and 1e), but most of the material formed is multilayer flakes as expected without special consideration devoted towards yielding single layer material.[32, 33] AFM images of the copper composite reveal correspondence between TEM imaging of the size distribution of the nanoparticles and the height distribution of the features observed by AFM (Figure 1f).

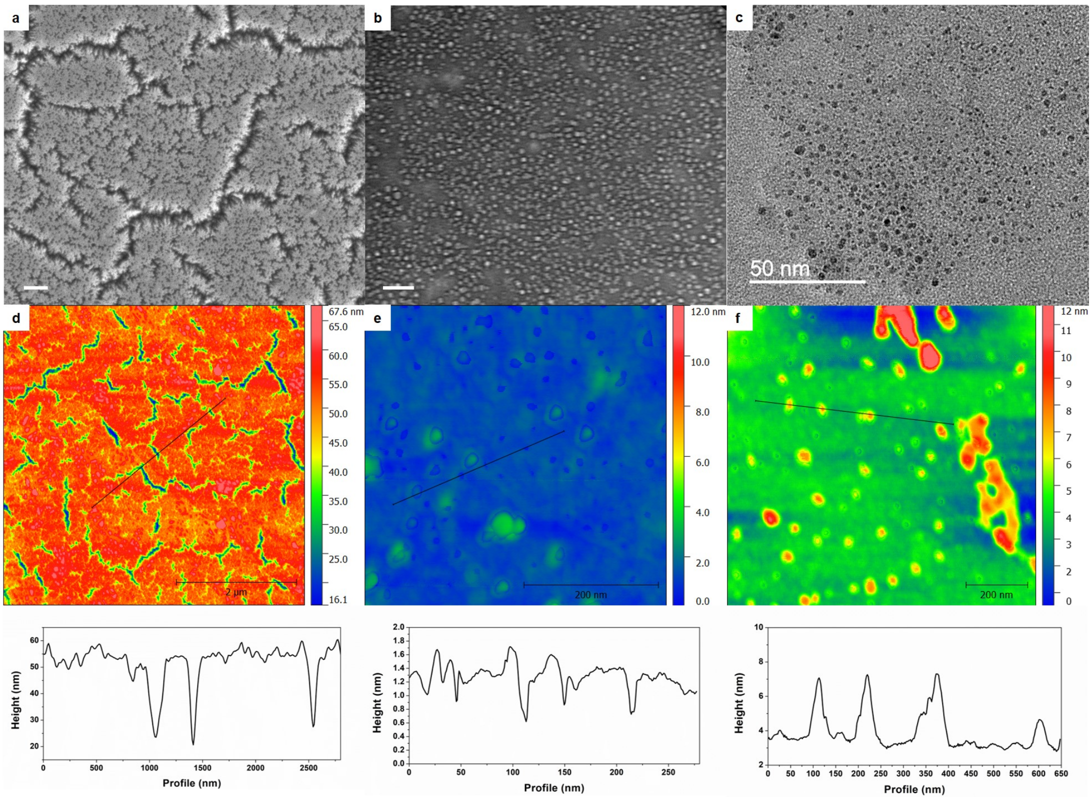

Figure 1: Electron microscopy and atomic force microscopy (AFM) characterization of the synthesis of GNCs. a) SEM of HOPG flake after RIE-COF-5 templated etching under optimized conditions (scale bar 200 nm). b) TEM of exfoliated HG sheet (scale bar 50 nm). c) HRTEM micrograph of HG copper nanoparticle composite utilizing optimized growth conditions (2 mg/mL of copper(II) chloride dihydrate). d) AFM of RIE-COF-5 templated etching. e) AFM of exfoliated HG sheet on mica. F) AFM of HG

copper nanoparticle composite on silicon wafer. (Height profiles for each AFM micrograph displayed below the respective micrograph).

Control experiments with no RIE failed to yield any exfoliation into water due to dissimilar surface energies of HOPG and water. RIE processing without COF templating yields material into water which is colloidally stable at lower concentrations but lacks the holey structure of COF-templated procedure (Figure S4). There are two primary differences between our synthesized material and this control experiment. For HOPG without COF-5 after RIE processing, the observed zeta potential was much larger, and the size of sheets was much smaller based on DLS and TEM (Figure S4 and S5). The contrast between the holey material and the RIE control is the difference between indiscriminate introduction of oxygen functionalities as compared to purposeful control of defects. While more oxygen functionalities will convey more colloidal stability, there is a lack of control in the resulting material and absence of larger sheets that are potentially useful in applications that require longer distance patterning.

Metal loading can be induced into the structures during a simple metal salt stirring procedure performed at room temperature in the dark. Precluding light is used to rule out the possibility of photoreduction reactions.[34] Introduction of nanoparticles into HG shows both concentration and time dependence. Holey graphene concentration before reactions is inferred from mass. Nanoparticle composites concentrations after reactions are determined by UV-vis absorption calibration curve (Figure S6). For this study we fixed the concentration of HG and varied the concentration of the metal salt. Briefly, a colloidally stable solution of HG was mixed with a range of metal salt (0.1 – 10 mg/mL) while stirring for a range of times (1 hour to 6 hours). Composites were recovered via centrifugation and washed several times with pure water to ensure removal of residual metal salt. Removal of metal salt was in general observed by UV-vis absorption spectroscopy (Figure S7). We envision widespread applications in catalysis due to the strong electronic coupling present between the introduced metal species and the underlying HG.

To elucidate the strong metal coupling between the HG and the metal nanoparticles, we performed a series of high resolution XPS experiments (Figure 2). High resolution carbon XPS reveals substantial differences of chemical moieties present in the as-exfoliated HG and each of the nanoparticle composites tested (Figure 2a). The as-exfoliated HG shows a substantial tail at higher binding energies as compared to the based sp^2 peak at 284 eV. We attributed these to a combination of oxygen moieties including hydroxyl, carbonyl, and ether functionalities. These observations are supported by FTIR of the HG which reveals similar features (Figure S8). Although each nanoparticle composite shows different sp^2 shifts, the consistent decrease of the intensity of higher binding energy tail features of the main peak indicates that these functionalities are either being coordinated by or consumed in the reduction of the nanoparticles. We attribute the mechanism of nanoparticle formation to oxidation of hydroxyl type functionalities located at the edges, which is confirmed by elimination of O-H related features in the IR spectra of GNCs (Figure S9). This is consistent with increased reactivity of edge-based moieties of graphene[35] and other previously reported nanoparticle reductions.[36]

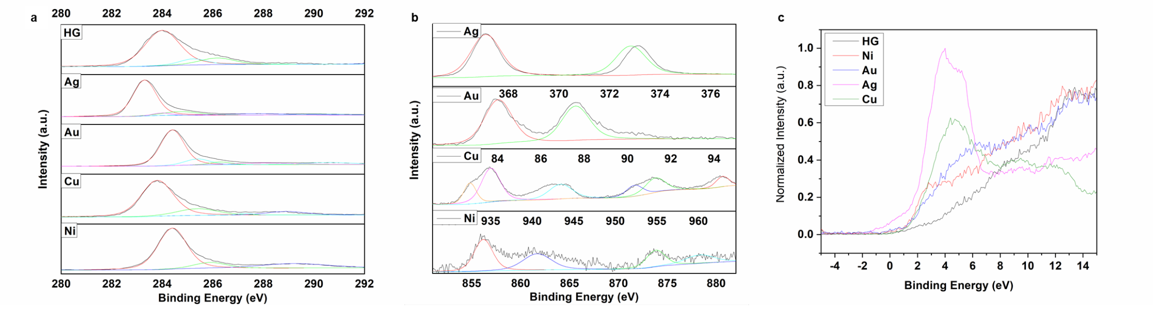

Figure 2: XPS of as-exfoliated HG and metal nanoparticle decorated GNCs. High resolution a) C1s, b) respective metal, and c) valence XPS scans of the HG and the different metal HG composites. Different colors in panels a) and b) represent deconvolutions of the overall signal into oxidation dependent peaks.

High resolution XPS of each of the relevant metal regions was taken to confirm the oxidation state and presence of the metals following the metal salt soaking procedure (Figure 2b). Both silver and gold GNCs demonstrate the presence of metal states (with 0 charge) in the expected regions. Silver additionally shows extensive nanoparticle formation (Figure S10). This promising decoration indicates the potential for easily fabricated and consistent surface enhanced Raman scattering (SERS) substrates that are unfortunately beyond the scope of the current work. Copper and nickel samples have relatively more complicated spectra that cannot be fitted with single oxidation states. Although identification of copper oxidation state by XPS is somewhat ambiguous, the presence of satellite peaks at 945 and 963 eV indicate copper(II) oxide being present.[37] The shoulder in the main peak at 935 eV would indicate the presence of a secondary oxidation state that could be copper(0) or copper(I). Additional HRTEM imaging reveals the presence of copper metal as well as copper(I) oxide by lattice fringe (Figure S11). No copper(II) oxide lattice fringes could be observed under HRTEM. Additionally, the presence of the oxide formation in the XPS experiment could be attributed to the deposition process used to prepare the samples. The evidence indicates that the copper present is a mixed valency species that is susceptible to oxidation under mild heating (<100°C). The presence of nickel hydroxide is confirmed by the relatively higher binding energy of the main peak at 857 eV. HRTEM of nickel GNC confirms the presence of nickel(0) lattice fringes as well but the same considerations for the copper hold here as well (Figure S12).

Valence XPS can be used as a tool to evaluate changes in the overall electronic structure of materials (Figure 2c). All metal composites show different valence structure than the as-exfoliated material. Prominently silver and copper HG composites show large d electron peaks and substantial shifts in the valence band edge as compared to HG. Both gold and nickel show some shift in valence band edge although the shifts are minor by comparison. Valence band shifts as compared to initial exfoliated material indicate that there are substantial electronic changes to the overall material occurring; suggestive of strong electronic coupling between the formed nanoparticles and the underlying HG. Resultant Fermi levels of the GNCs are consistent with an averaging of workfunctions between the HG and the metal (Figure S13).

Resulting nanoparticle size shows a sensitive metal precursor concentration dependence which is best illustrated through TEM (Figure 3) but also supported through UV-vis absorption spectroscopy (Figure S14). Initially at higher concentrations of the metal precursor, formation of reduced structures completely overwhelms the size confining ability of the patterned holes (Figure 3a). Overwhelming the patterned holes of all composites holds albeit with different concentrations for different metal precursors. As the concentration is decreased (Figure 3b), nanoparticle overgrowth can still be observed but some of the size defining effect of the patterned holes can be observed as discrete structures can be resolved. Further decrease in metal precursor concentration can yield well defined nanoparticles that show little to no overgrowth (Figure 3c). Additional decrease in metal precursor concentration shows no additional benefits and less overall nanoparticle formation at a given time point (Figure S15). Although these observations are for concentrations at a relatively short time point (1 hour), The overall size limiting behavior is observed for the optimized concentration persists into long time points with more complete decoration (Figure S16).

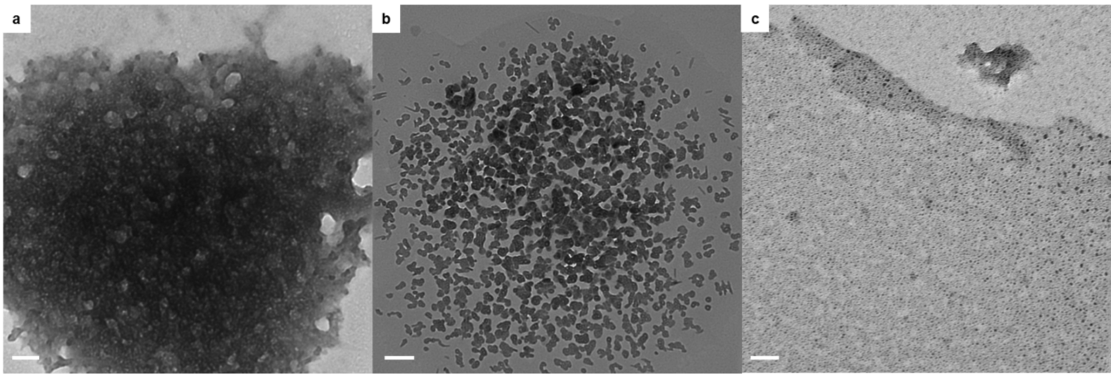

Figure 3: TEM micrographs of different copper HG composite syntheses at progressively lower ratios of copper(II) chloride to HG (0.146 mg/mL). a) 5 mg/mL of $CuCl_2$ HG (scale bar 100 nm). b) 2.5 mg/mL of $CuCl_2$ HG (scale bar 200 nm). c) 2 mg/mL of $CuCl_2$ HG (scale bar 50 nm).

HRTEM micrographs can be used to clarify the identity and oxidation state of the nanoparticles present in the composites (Figure 4). Both more positive reduction potential metals, silver and gold, the composites show small nanoparticles with lattice spacing that can be indexed to the metal(0) oxidation state (Figure 4a and 4b). Both single orientation of lattice spacing and multiple different lattice spacing growing together can be observed in the micrographs. Variability in lattice orientation indicates that the holes can support the growth of a single nanoparticle with a single nucleation site or multiple nucleation sites form around the hole and grow into a single nanoparticle. Although many nanoparticles are spaced relatively far apart as compared to the dimensions of the COF, there are several instances where nanoparticles are within a few nanometers of each other. Small inter-nanoparticle distances are relevant for a variety of technical applications which are currently underexplored due to the difficulty of placing nanoparticles in proximity. HG could serve as a route to these underexplored regimes. Further examination of the lattice spacing of the relatively negative reduction potential metals, copper and nickel, reveal more complex lattice spacing that cannot be attributed to single oxidation states (Figure 4c, 4d, S11, and S12). This behavior is somewhat expected as even if the nanoparticles were prepared in a metal(0) state, both metals are much more prone to oxidation than silver or gold species.

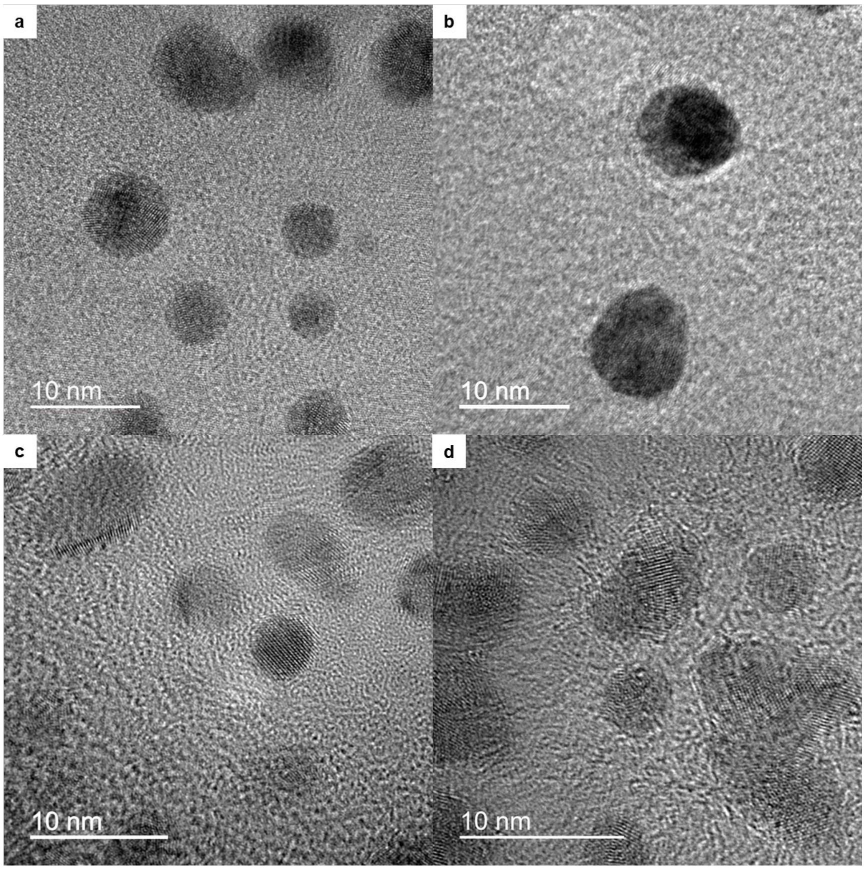

Figure 4: HRTEM micrographs of a) silver, b) gold, c) copper, and d) nickel decorated GNCs using optimized conditions for growth.

Zeta potential and dynamic light scattering (DLS) were also measured to evaluate both the stability and size distributions of both the initial exfoliated material as well as the material after metal decoration (Figure S17-21). HG is colloidally stable at lower concentrations (0.059 mg/mL zeta potential of –30.1 ± 10.2 mV) due to the abundance of oxygen containing functional groups introduced during the RIE process. DLS reveals two distinct size distributions centered around 150 nm and 950 nm indicating a range of material in solution. Each of the other composite materials zeta potential and size distributions show somewhat different behavior as compared to the HG. The primary distinction is the reduction of smaller size flakes and retention of a negative zeta potential albeit at varying magnitudes. The limiting of the small size distributions can be attributed to the effect of centrifugation as part of the composite synthesis. As only the pellet is resuspended, we can expect a shifting towards material that is more easily precipitated. The negative zeta potential can be ascribed to the retention of anionic salts to act as weakly bound ligands to composites nanoparticles. The relatively weakly bound nature of these ligands should ensure that they can be removed for catalytical applications as needed.

Computational investigations based on density functional theory (DFT) are used to understand the effects of inclusion of the nanoparticles in the HG and on the electronic structure of the composite. Gold clusters are chosen as the main model system, since Au-GNC samples demonstrate higher heterogeneity in their oxidation state and zeta-potential (Figure 2b and S19). The size of the synthesized systems is computationally prohibitive, therefore a smaller magic-size gold cluster[38-42] of 13 atoms in size, Au_{13}, is used as a simplified model of a metal nanoparticle. Au_{13} is inserted into the 1.5 nm hole at the HG, as illustrated in Figure 5a-5c. The lattice structure of Au_{13} perfectly fits to the geometry of the hole at the HG model. The edges of the hole at the HG model are capped by hydrogens and six carboxyl groups (Figure 5b). It is expected that substitution of OH groups by H capping groups have a negligible effect on the electronic structure of the HG. This trend was observed for covalently functionalized carbon nanotubes (CNT), where substitution of OH groups with H at the sp^3-defect side negligibly altered the electronic structure[43,44,45] of the CNT. Figure S22 evidences that the HG capped with OH and 6 COOH has similar electronic features as the DOS of the HG with 6 COOH and the hydrogenated capping. Therefore, for simplicity, only the models with hydrogenated edges are used in calculations. This choice of the capping model is also rationalized by the fact that OH features in IR spectra are not resolved for Au-GNCs (Figure S9). Therefore, it is reasonable to assume that hydroxyl groups do not contribute to the coordination of Au nanoparticle and are not expected to critically affect their electronic structure.

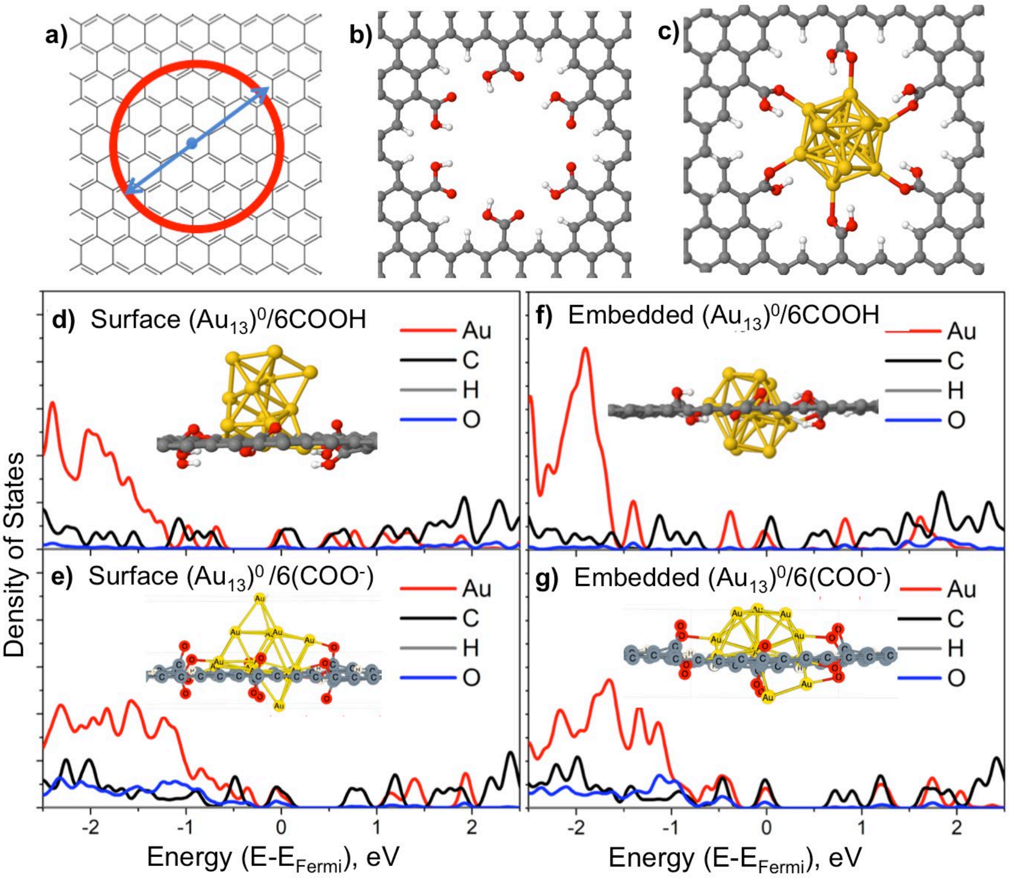

Figure 5: Schematic representation **(a)** and optimized structures of the HG model **(b)** and HG with the gold cluster, Au_{13}, embedded inside the hole of HG **(c)**. The density of states (DOS) projected to the orbitals associated with carbon (black lines), oxygen (blue lines), hydrogen (grey lines), and gold (red lines) atoms of the HG with embedded $(Au_{13})^0$ coordinated with 6(COOH) **(d)** and 6(COO^-) **(e)** and with the $(Au_{13})^0$ at the surface of the hole coordinated with 6(COOH) **(f)** and 6(COO^-) **(g)**. The negative charge of the whole system corresponds to the number of deprotonated carboxyl groups. Inserts show the optimized structures of the embedded and surface conformations.

Due to flexibility of carboxyl groups, the Au_{13} cluster can be embedded inside the hole or slightly above the hole (at the surface), while strongly coordinated by carboxyl groups in both cases (Figure 5). Since carboxyl groups can be easily deprotonated in water solutions, we consider the “embedded” and “surface” structures for two cases: (i) HG with fully protonated carboxyl groups and zero charge on the metal cluster, $(Au_{13})^0/6COOH$, and (ii) HG with deprotonated groups turning to carboxylates, while the metal cluster remaining neutral, $(Au_{13})^0/6(COO^-)$. The number of deprotonated groups dictates the overall charge of the system. As such, the negative charge of deprotonated models is consistent with slightly negative zeta potential obtained experimentally for Au-GNCs (Figure S19).

Figure 5d-5g show the density of states (DOS) projected on the orbitals originated from carbon, oxygen, and, metal atoms for embedded and surface structures of the neutral gold cluster coordinated with six carboxyl groups and six carboxyl groups being deprotonated. In all cases, the gold cluster introduces the metal-associated states at the Fermi energy. While these states are significantly hybridized with the carbon-originated states, the pristine HG does not exhibit states directly at the Fermi energy (Figure S22 and S23). The embedded protonated and deprotonated structures contribute additional Au-originated states at the edge of the VB from –0.5 eV to 0 eV (Figure 5f and 5g). In contrast, the surface $(Au_{13})^0/6COOH$ has a well-pronounced sub-gap at this energy range. Interestingly, deprotonated carboxyl groups in the surface structure facilitate penetration of the gold cluster inside the HG, making it look more like the embedded conformation (inserts in Figure 5e and 5g). As a result, the peaks at the VB of the surface $(Au_{13})^0/6(COO^-)$ are similar to those of the embedded $(Au_{13})^0/6(COO^-)$ system. Overall, deprotonation of carboxyl groups leads to their stronger coordination with the embedded metal cluster, which broadens and shifts the metal-associated peaks toward the edge of the VB.

Comparing these calculated results to the experimental valence XPS scans of the HG and the Au-HG composites in Figure 2c, we can conclude that only the embedded $(Au_{13})^0$ cluster provides distinct peaks in the VB edge compared to HG, which agrees with experimental data. As such, we suggest that the nanoparticle is formed completely embedded in the hole of the HG, rather than at the surface of the hole. Second, the nanoparticle is expected to have no charge, while coordinated by fully protonated carboxyl groups. Figure S24 evidences that the structure with the positively charged cluster coordinated to six deprotonated carboxyl groups, $(Au_{13})^{6+}/6(COO^-)$, exhibits a sub-gap at the edge of the VB from –1 eV to 0 eV, with the metal-associated peak at the Fermi energy, which does not agree with the electronic features observed experimentally (Figure 2c).

The calculations of the DOS of embedded $(Ag_{13})^0$ and $(Cu_{13})^0$ clusters, that were constructed in a similar manner as embedded $(Au_{13})^0$, also demonstrate a well-pronounced metal-associated peak at the edge of the VB that is distinct from the VB edge of HG (Figure S23). All embedded clusters show very similar VB near the Fermi-energy, while the difference in their bands become more noticeable for states deeper inside the VB, especially for d-states associated with metals. Deprotonation of all carboxylic groups coordinated with metal clusters results in a slight redshift (~0.5 eV) of the highly intensive peaks associated with metal d-d orbitals, broadening their shapes near to the VB edge (Figures S25-S27). This broadening is the most pronounced for $(Ag_{13})^0/6(COO^-)$ system. Taking into account that the zeta potential of Ag-HG composites shows a wider distribution toward more negative values compared to those of Au-HG and Cu-HG (Figures S15-S17), it is reasonable to assume that structures with deprotonated carboxyl groups are more frequently present in Ag-HG samples. These deprotonated structures are likely result in much more pronounced VB shoulder at the lowest energies observed for Ag-HG, compared to other composites, Figure 2c.

To evaluate these GNCs as electrocatalytic platforms, we investigated the activity of the Ni-GNC for oxygen evolution reaction (OER) activity (Figure 6). GNCs can serve as a platform to reduce overall metal usage, provide additional conductivity to boost catalytical activity, and reduce sintering.

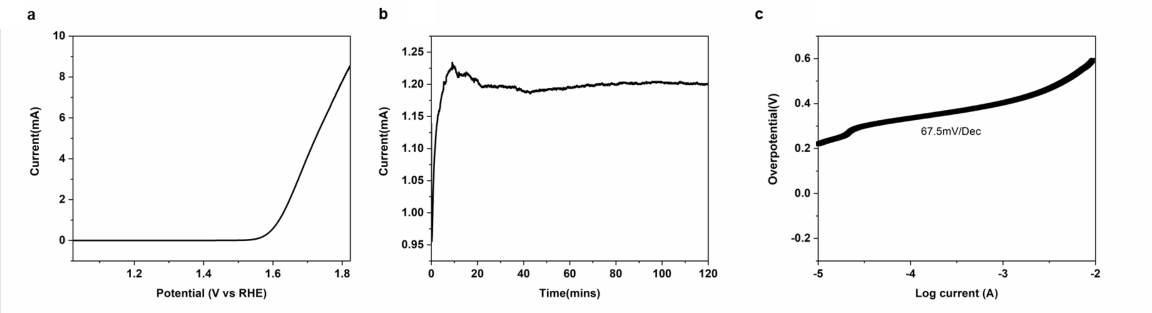

Figure 6: Electrochemical catalytic data for Ni-GNC toward oxygen evolution reaction (OER). a) Linear sweep voltammogram (LSV) in 1 M KOH on a rotating disk electrode @ 1600 rpm. b) Galvanostatic electrolysis of Ni-GNCs for 2 hours of continuous operation under the same conditions as LSV. c) Tafel plot of a) where the central region has been fitted.

Current of 5 mA can be seen at 1.7 V potential vs RHE for 80 µg of Ni-GNC deposited onto a glassy carbon electrode (Figure 6a). Onset potential for catalysis is at 1.53 V vs RHE, on par with other $Ni(OH)_2$ based OER catalysts.[46, 47] Catalytic activity shows stability over 2 hours of continuous operation at 1.6 V vs RHE (Figure 6b). This performance serves as indirect evidence of the stability of the nanoparticles to remain inside of the holes and avoid sintering. Tafel slope of the Ni-GNC composite is 67.5 mV/dec, the value is also consistent with other $Ni(OH)_2$ based catalysts. Electrochemical impedance spectroscopy was used to evaluate both surface area and the favorability of charge transfer after the onset potential (Figure S28). Equivalent circuit modeling at open circuit potential (1.28 V vs RHE) reveals large resistance to charge transfer (22570 Ohms) and 20 μF capacitance. Similar capacitances were observed under working potentials of 1.6 V and 1.7 V vs RHE but with dramatically reduced charge transfer resistance (193 and 133 Ohms, respectively). Additional confirmation of capacitance values was obtained by differential scanning of cyclic voltammetry in a 0.05 V non-faradaic window around 1.28 V vs RHE (Figure S29). Assuming a specific capacitance of 40 $\mu F/cm^2$ in 1 M KOH, the overall electrochemically active surface area is approximately 0.61 cm^2.[48] We attribute the relatively small area to preference for restacking during deposition on electrode as well as the presence of Nafion in the catalyst ink blocking active sites. Future studies will focus on improving the active area but are beyond the scope of this current work. Further improvements in onset potential could be induced through pre- and post-synthetic doping strategies to generate Ni-Fe hybrids.[49, 50]

Conclusion:

Here we have demonstrated a facile process for production of holey graphene from HOPG via a COF-5 RIE process. The resulting material can be exfoliated into water and can have flake sizes ranging from 1 to 2 micrometers densely patterned with nanometer sized features. The material is active for a broad reduction potential range of size limited nanoparticles dictated by the relative ratio of metal salt to HG. Both metal(0) and metal oxide/hydroxide states were observed to form in an element dependent fashion without additional reducing agents. Edge hydroxyl-based oxidation is posited as the reduction mechanism as per FTIR and XPS evidence. Formed composites demonstrated strong electronic coupling between carbon and metal resulting in large changes to carbon and valence XPS of the material. Nanoparticle growth can overwhelm the hole sites at higher concentrations forming larger agglomerations. At lower concentrations metal nanoparticles can remain contained in their respective sites and cover large areas of the HG. All composite materials form metastable suspensions in water with negative zeta potentials, which we associate to the retention of anionic ligands, including deprotonated carboxyl groups at the HG edges, weakly coordinated to the nanoparticles in the composites. Computational investigations on model systems reveal a preference for embedding of nanoparticles inside the hole of the HG over their surface-based incorporation. Metal d-states are shown to contribute to the valence band of the electronic structure only for neutral nanoparticles consistent with XPS evidence. Ni-GNCs were evaluated as OER catalysts and demonstrated low overpotential of 300 mV, no degradation of current over two hours of operation, and 67.5 mV/dec Tafel slope.

Experimental:

COF-5 Growth on HOPG

COF-5 was synthesized following a previously published procedure.[30] Briefly, a thick walled glass container was cleaned and dried in an oven. A mixture of phenylbisboronic acid (PBBA) (6.25 mg, 37.7 mmol) and 2,3,6,7,10,11-hexahydroxytriphenylene (HHTP) (4.00 mg, 12.33 mmol) in 1:1 mixture of 1 total mL of 1,4-dioxane and mesitylene was added to the container and sonicated for 30 minutes. After sonication, 1×1 cm flakes of freshly cleaved highly ordered pyrolytic graphite (HOPG, #439HP-AB from SPI Supplies, West Chester, PA) were introduced to the vessel and left in an oven at 90°C for 40 minutes. The reaction vessel was allowed to cool to room temperature before removing the HOPG flakes and placing them in toluene overnight. The powder was washed with toluene and recovered via vacuum filtration. Substrates were sonicated the next day in toluene for 10 seconds and then placed in vacuum to thoroughly dry for several hours.

Reactive ion etching

Trion Phantom III LT RIE was used to etch HOPG flakes. The following conditions were used for etching: 200 mTorr pressure with 100 W of power for 30 seconds and 50 sccm of O_2 flow were chosen as the final conditions. After etching, the substrates were washed with ethanol, nanopure water, and ethanol again to remove residual polymer. HOPG flakes were dried in vacuum after the wash to retrieve an initial starting mass used to estimate concentration in solution.

Exfoliation into solution

Dried patterned HOPG flakes were massed and then placed into 2 mL of nanopure water in a 1-dram vial. Sonication proceeded for 3 hours to attempt maximal retrieval of patterned material. After sonicating, the solution was retrieved and placed into a separate 1-dram vial for storage. The flake (if remaining) would be retrieved and dried under vacuum for several hours before massing. The mass difference between before and after sonication was used to estimate concentration in solution.

Nanoparticle formation

Solutions of HG were diluted to 0.292 mg/mL and mixed with a variety of metal salt solutions at different concentrations. The following metal salts were used: $AgNO_3$, $HAuCl_4 \cdot 3H_2O$, $CuCl_2 \cdot 2H_2O$, and $NiCl_2 \cdot 6H_2O$. Concentrations ranged from 10 mg/mL to 0.1 mg/mL. The typical copper process was to introduce 1 mL of 0.292 mg/mL HG to 1 mL of 4 mg/mL metal salt solution in a 1-dram vial with a freshly cleaned stir bar. The magnetic stirrer was set at 800 rpm and the reaction was carried out in the dark at room temperature. All screening conditions for nanoparticle decoration were conducted with 1-hour reaction while more complete coverage of nanoparticles was achieved with 6-hour reactions. After the reaction was completed, the solutions were centrifuged down for 30 minutes. The supernatant was recovered and 2 mL of nanopure water were added for an additional two centrifugations. The later supernatants were discarded, and the final solutions were brought up in 1 mL of nanopore water in a 1-dram vial. Optimized conditions for all metal salts were as follows: (Au) 2.5 mg/mL, (Ag) 5 mg/mL, (Cu) 4 mg/mL, and (Ni) 10 mg/mL.

Computational methodology

All DFT calculations were performed in the Vienna Ab-initio Simulation Package[51-53] (VASP 5.4.4) using the Perdew, Burke, and Ernzerhof (PBE)[54] exchange-correlation generalized gradient approximation (GGA) functional with projector-augmented wave (PAW) pseudopotentials[55, 56] and plane-wave basis sets at the Gamma k-point. The supercell of HG with metal clusters is 20 Å × 21.5 Å along the x-y plane, where the z dimension varies, while providing at least 8 Å separation to minimize spurious interactions between replicas. The charge of the whole system is determined by the number of deprotonated carboxyl groups, while the charge on the metal cluster is zero. The optimization of the metal-HG systems was performed till the forces between ions were smaller than 0.01 eV/Å. All projected density of states (PDOS) calculations were performed at the Gamma-point. The $(Ag_{13})^0$ and $(Cu_{13})^0$ clusters were embedded in the HG with hydrogenated edges and coordinated to protonated or deprotonated carboxyl groups, similar to the created structures of the emended $(Au_{13})^0$ cluster. Then the metal-HG structures are optimized at the same size supercell using the same methodology as Au-HG.

ASSOCIATED CONTENT

Supporting Information. The following files are available free of charge.

Additional details on experimental methods. Figures for electron microscopy of as-patterned HOPG, RIE screening conditions, RIE without COF control experiments, Ag-GNC, Cu-GNC, Ni-GNC, Low salt and longer time Cu-GNC, Raman spectra of screening conditions, XPS metal-based metal loadings, Valence XPS comparison of HG, GNCs and metal references, UV-Vis calibration curve of HG, post-wash GNCs, and different Cu metal conditions for Cu-GNC, FTIR spectra of HG and resulting GNCs, DLS/zeta potential for RIE control, HG, and all GNCs, DFT calculations of metal clusters and density of states. Electrochemical impedance spectroscopy and cyclic voltammetry.

AUTHOR INFORMATION

Corresponding Author

Alexander Star

Email: astar@pitt.edu

Author Contributions

The manuscript was written through contributions of all authors. All authors have given approval to the final version of the manuscript.

Funding Sources

This material is based upon work supported by the National Science Foundation under Grant No. 2003302.

Notes

ACKNOWLEDGMENT

The XplorA Raman-AFM/TERS system was purchased via Defense University Research Instrumentation Program (DURIP) grant from the Office of Naval Research, ONR (N000141410765). We would additionally like to acknowledge Douglas R. Kauffman for helpful discussions regarding experiments.

References

1. Zhu, Y.; Murali, S.; Cai, W.; Li, X.; Suk, J. W.; Potts, J. R.; Ruoff, R. S., Graphene and Graphene Oxide: Synthesis, Properties, and Applications. *Adv. Mater.* **2010,** *22*, 3906-3924.
2. Chen, Q.; Zhang, L.; Chen, G., Facile Preparation of Graphene-Copper Nanoparticle Composite by in situ Chemical Reduction for Electrochemical Sensing of Carbohydrates. *Anal. Chem.* **2012,** *84*, 171-178.
3. Liu, J.; Ma, Q.; Huang, Z.; Liu, G.; Zhang, H., Recent Progress in Graphene-Based Noble-Metal Nanocomposites for Electrocatalytic Applications. *Adv. Mater.* **2019,** *31*, e1800696.
4. Jo, G.; Choe, M.; Lee, S.; Park, W.; Kahng, Y. H.; Lee, T., The Application of Graphene as Electrodes in Electrical and Optical Devices. *Nanotechnology* **2012,** *23*, 112001-112012.
5. Georgakilas, V.; Tiwari, J. N.; Kemp, K. C.; Perman, J. A.; Bourlinos, A. B.; Kim, K. S.; Zboril, R., Noncovalent Functionalization of Graphene and Graphene Oxide for Energy Materials, Biosensing, Catalytic, and Biomedical Applications. *Chem. Rev.* **2016,** *116*, 5464-5519.
6. Novoselov, K. S.; Fal'ko, V. I.; Colombo, L.; Gellert, P. R.; Schwab, M. G.; Kim, K., A Roadmap for Graphene. *Nature* **2012,** *490*, 192-200.
7. Ehsani, A.; Heidari, A. A.; Shiri, H. M., Electrochemical pseudocapacitors based on ternary nanocomposite of conductive polymer/graphene/metal oxide: An introduction and review to it in recent studies. *Chem. Rec.* **2019,** *19*, 908-926.
8. Ajdari, F. B.; Kowsari, E.; Ehsani, A.; Schorowski, M.; Ameri, T., New synthesized ionic liquid functionalized graphene oxide: synthesis, characterization and its nanocomposite with conjugated polymer as effective electrode materials in an energy storage device. *Electrochim. Acta* **2018,** *292*, 789-804.
9. Ehsani, A.; Kowsari, E.; Ajdari, F. B.; Safari, R.; Shiri, H. M., Sulfonated graphene oxide and its nanocomposites with electroactive conjugated polymer as effective pseudocapacitor electrode materials. *J. Colloid Interface Sci.* **2017,** *497*, 258-265.
10. Higgins, D.; Zamani, P.; Yu, A.; Chen, Z., The Application of Graphene and its Composites in Oxygen Reduction Electrocatalysis: a Perspective and Review of Recent Progress. *Energy Environ. Sci.* **2016,** *9*, 357-390.
11. Kou, R.; Shao, Y.; Mei, D.; Nie, Z.; Wang, D.; Wang, C.; Viswanathan, V. V.; Park, S.; Aksay, I. A.; Lin, Y., Stabilization of Electrocatalytic Metal Nanoparticles at Metal− Metal Oxide− Graphene Triple Junction Points. *J. Am. Chem. Soc.* **2011,** *133*, 2541-2547.
12. Li, Y.; Zhou, W.; Wang, H.; Xie, L.; Liang, Y.; Wei, F.; Idrobo, J. C.; Pennycook, S. J.; Dai, H., An Oxygen Reduction Electrocatalyst Based on Carbon Nanotube-Graphene Complexes. *Nat. Nanotechnol.* **2012,** *7*, 394-400.
13. Liang, Y.; Li, Y.; Wang, H.; Zhou, J.; Wang, J.; Regier, T.; Dai, H., Co 3 O 4 Nanocrystals On Graphene as a Synergistic Catalyst for Oxygen Reduction Reaction. *Nat. Mat.* **2011,** *10*, 780.
14. Dou, S.; Tao, L.; Huo, J.; Wang, S.; Dai, L., Etched and Doped Co 9 S 8/Graphene Hybrid for Oxygen Electrocatalysis. *Energy Environ. Sci.* **2016,** *9*, 1320-1326.

15. Li, J. S.; Wang, Y.; Liu, C. H.; Li, S. L.; Wang, Y. G.; Dong, L. Z.; Dai, Z. H.; Li, Y. F.; Lan, Y. Q., Coupled Molybdenum Carbide and Reduced Graphene Oxide Electrocatalysts for Efficient Hydrogen Evolution. *Nat. Commun.* **2016,** *7*, 11204.

16. Li, Y.; Li, Y.; Zhu, E.; McLouth, T.; Chiu, C. Y.; Huang, X.; Huang, Y., Stabilization of High-Performance Oxygen Reduction Reaction Pt Electrocatalyst Supported on Reduced Graphene Oxide/Carbon Black Composite. *J. Am. Chem. Soc.* **2012,** *134*, 12326-12329.

17. Liang, Y.; Li, Y.; Wang, H.; Dai, H., Strongly Coupled Inorganic/Nanocarbon Hybrid Materials for Advanced Electrocatalysis. *J. Am. Chem. Soc.* **2013,** *135*, 2013-2036.

18. Wang, H.; Dai, H., Strongly Coupled Inorganic-Nano-Carbon Hybrid Materials for Energy Storage. *Chem. Soc. Rev.* **2013,** *42*, 3088-3113.

19. Yang, S.; Zhi, L.; Tang, K.; Feng, X.; Maier, J.; Müllen, K., Efficient Synthesis of Heteroatom (N Or S)-Doped Graphene Based on Ultrathin Graphene Oxide-Porous Silica Sheets for Oxygen Reduction Reactions. *Adv. Funct.Mater.* **2012,** *22*, 3634-3640.

20. Wang, X.; Sun, G.; Routh, P.; Kim, D. H.; Huang, W.; Chen, P., Heteroatom-Doped Graphene Materials: Syntheses, Properties and Applications. *Chem. Soc. Rev.* **2014,** *43*, 7067-7098.

21. Zheng, Y.; Jiao, Y.; Ge, L.; Jaroniec, M.; Qiao, S. Z., Two-Step Boron and Nitrogen Doping in Graphene for Enhanced Synergistic Catalysis. *Angew. Chem. Int. Ed .Engl.* **2013,** *52*, 3110-3116.

22. Peng, G.; Ellis, J. E.; Xu, G.; Xu, X.; Star, A., In Situ Grown TiO2 Nanospindles Facilitate the Formation of Holey Reduced Graphene Oxide by Photodegradation. *ACS Appl. Mater. Interfaces* **2016,** *8*, 7403-7410.

23. Hu, X.; Bai, D.; Wu, Y.; Chen, S.; Ma, Y.; Lu, Y.; Chao, Y.; Bai, Y., A Facile Synthesis of Reduced Holey Graphene Oxide for Supercapacitors. *Chem. Commun. (Camb)* **2017,** *53*, 13225-13228.

24. Zhao, X.; Hayner, C. M.; Kung, M. C.; Kung, H. H., Flexible Holey Graphene Paper Electrodes with Enhanced Rate Capability for Energy Storage Applications. *ACS Nano* **2011,** *5*, 8739-8749.

25. Xu, Y.; Lin, Z.; Zhong, X.; Huang, X.; Weiss, N. O.; Huang, Y.; Duan, X., Holey Graphene Frameworks for Highly Efficient Capacitive Energy Storage. *Nat. Commun.* **2014,** *5*, 4554.

26. Lin, Y.; Han, X.; Campbell, C. J.; Kim, J. W.; Zhao, B.; Luo, W.; Dai, J.; Hu, L.; Connell, J. W., Holey Graphene Nanomanufacturing: Structure, Composition, and Electrochemical Properties. *Adv.Funct. Mater.* **2015,** *25*, 2920-2927.

27. Han, X.; Funk, M. R.; Shen, F.; Chen, Y. C.; Li, Y.; Campbell, C. J.; Dai, J.; Yang, X.; Kim, J. W.; Liao, Y.; Connell, J. W.; Barone, V.; Chen, Z.; Lin, Y.; Hu, L., Scalable Holey Graphene Synthesis and Dense Electrode Fabrication Toward High-Performance Ultracapacitors. *ACS Nano* **2014,** *8*, 8255-8265.

28. Xu, Y.; Chen, C. Y.; Zhao, Z.; Lin, Z.; Lee, C.; Xu, X.; Wang, C.; Huang, Y.; Shakir, M. I.; Duan, X., Solution Processable Holey Graphene Oxide and Its Derived Macrostructures for High-Performance Supercapacitors. *Nano Lett.* **2015,** *15*, 4605-4610.

29. Li, H.; Chavez, A. D.; Li, H.; Li, H.; Dichtel, W. R.; Bredas, J. L., Nucleation and Growth of Covalent Organic Frameworks from Solution: The Example of COF-5. *J. Am. Chem. Soc.* **2017,** *139*, 16310-16318.

30. White, D. L.; Burkert, S. C.; Hwang, S. I.; Star, A., Holey Graphene Metal Nanoparticle Composites via Crystalline Polymer Templated Etching. *Nano Lett.* **2019,** *19*, 2824-2831.

31. Wu, J. B.; Lin, M. L.; Cong, X.; Liu, H. N.; Tan, P. H., Raman Spectroscopy of Graphene-Based Materials and Its Applications In Related Devices. *Chem. Soc. Rev.* **2018,** *47*, 1822-1873.

32. Bepete, G.; Anglaret, E.; Ortolani, L.; Morandi, V.; Huang, K.; Penicaud, A.; Drummond, C., Surfactant-Free Single-Layer Graphene in Water. *Nat. Chem.* **2017,** *9*, 347-352.

33. Haar, S. b.; Bruna, M.; Lian, J. X.; Tomarchio, F.; Olivier, Y.; Mazzaro, R.; Morandi, V.; Moran, J.; Ferrari, A. C.; Beljonne, D., Liquid-Phase Exfoliation of Graphite Into Single-and Few-Layer Graphene With α-Functionalized Alkanes. *J. Phys. Chem. Lett.* **2016,** *7*, 2714-2721.

34. Henglein, A., Colloidal Silver Nanoparticles: Photochemical Preparation and Interaction with O2, CCl4, and Some Metal Ions. *Chem. Mater.* **1998,** *10*, 444-450.

35. Sharma, R.; Baik, J. H.; Perera, C. J.; Strano, M. S., Anomalously Large Reactivity of Single Graphene Layers and Edges Toward Electron Transfer Chemistries. *Nano Lett.* **2010,** *10*, 398-405.

36. Raj, M. A.; John, S. A., Assembly of Gold Nanoparticles on Graphene Film Via Electroless Deposition: Spontaneous Reduction of Au 3+ Ions by Graphene Film. *RSC Advances* **2015,** *5*, 4964-4971.

37. Briggs, D., Practical Surface Analysis. *Auger and X-Ray Photoelecton Spectroscory* **1990,** *1*, 151-152.

38. Menard, L. D.; Xu, F.; Nuzzo, R. G.; Yang, J. C., Preparation of TiO2-Supported Au Nanoparticle Catalysts From a Au13 Cluster Precursor: Ligand Removal Using Ozone Exposure Versus a Rapid Thermal Treatment. *J. Catal.* **2006,** *243*, 64-73.

39. Shichibu, Y.; Konishi, K., HCl-Induced Nuclearity Convergence in Diphosphine-Protected Ultrasmall Gold Clusters: A Novel Synthetic Route to "Magic-Number" Au13 Clusters. *Small* **2010,** *6*, 1216-1220.

40. Okumura, M.; Kitagawa, Y.; Kawakami, T.; Haruta, M., Theoretical Investigation of the Hetero-Junction Effect in PVP-Stabilized Au13 Clusters. The Role of PVP in Their Catalytic Activities. *Chem. Phys. Lett.* **2008,** *459*, 133-136.

41. Larsson, J.; Nolan, M.; Greer, J. C., Interactions Between Thiol Molecular Linkers and the Au13 Nanoparticle. *J. Phys. Chem. B* **2002,** *106*, 5931-5937.

42. Shichibu, Y.; Konishi, K., HCl‐Induced Nuclearity Convergence in Diphosphine‐Protected Ultrasmall Gold Clusters: A Novel Synthetic Route to “Magic‐Number” Au13 Clusters. *Small* **2010,** *6*, 1216-1220.

43. Gifford, B. J.; Kilina, S.; Htoon, H.; Doorn, S. K.; Tretiak, S., Exciton Localization and Optical Emission in Aryl-Functionalized Carbon Nanotubes. *J. Phys. Chem. C* **2017,** *122*, 1828-1838.

44. He, X.; Gifford, B. J.; Hartmann, N. F.; Ihly, R.; Ma, X.; Kilina, S. V.; Luo, Y.; Shayan, K.; Strauf, S.; Blackburn, J. L.; Tretiak, S.; Doorn, S. K.; Htoon, H., Low-Temperature Single Carbon Nanotube Spectroscopy of sp(3) Quantum Defects. *ACS Nano* **2017,** *11*, 10785-10796.

45. Saha, A.; Gifford, B. J.; He, X.; Ao, G.; Zheng, M.; Kataura, H.; Htoon, H.; Kilina, S.; Tretiak, S.; Doorn, S. K., Narrow-Band Single-Photon Emission Through Selective Aryl Functionalization of Zigzag Carbon Nanotubes. *Nat. Chem.* **2018,** *10*, 1089-1095.

46. Wang, L.; Chen, H.; Daniel, Q.; Duan, L.; Philippe, B.; Yang, Y.; Rensmo, H.; Sun, L., Promoting the Water Oxidation Catalysis by Synergistic Interactions between Ni(OH)2and Carbon Nanotubes. *Adv. Energy Mater.* **2016,** *6*, 1600516.

47. Guo, X.; Kong, R.-M.; Zhang, X.; Du, H.; Qu, F., Ni(OH)2 Nanoparticles Embedded in Conductive Microrod Array: An Efficient and Durable Electrocatalyst for Alkaline Oxygen Evolution Reaction. *ACS Catalysis* **2017,** *8*, 651-655.

48. McCrory, C. C.; Jung, S.; Peters, J. C.; Jaramillo, T. F., Benchmarking heterogeneous electrocatalysts for the oxygen evolution reaction. *J. Am. Chem. Soc.* **2013,** *135*, 16977-16987.

49. Klaus, S.; Cai, Y.; Louie, M. W.; Trotochaud, L.; Bell, A. T., Effects of Fe Electrolyte Impurities on Ni(OH)2/NiOOH Structure and Oxygen Evolution Activity. *J. Phys. Chem. C* **2015,** *119*, 7243-7254.

50. Ren, J. T.; Yuan, G. G.; Weng, C. C.; Chen, L.; Yuan, Z. Y., Uniquely Integrated Fe-Doped Ni(OH)2 Nanosheets for Highly Efficient Oxygen and Hydrogen Evolution Reactions. *Nanoscale* **2018,** *10*, 10620-10628.

51. Kresse, G.; Hafner, J., Ab Initio Molecular Dynamics For Liquid Metals. *Phys. Rev. B Condens. Matter.* **1993,** *47*, 558-561.

52. Kresse, G.; Hafner, J., Ab Initio Molecular-Dynamics Simulation of the Liquid-Metal-Amorphous-Semiconductor Transition in Germanium. *Phys. Rev. B Condens. Matter* **1994,** *49*, 14251-14269.

53. Kresse, G.; Furthmüller, J., Efficiency of Ab-Initio Total Energy Calculations for Metals and Semiconductors Using a Plane-Wave Basis Set. *Comput. Mater. Sci.* **1996,** *6*, 15-50.

54. Perdew, J. P.; Burke, K.; Ernzerhof, M., Generalized Gradient Approximation Made Simple. *Phys. Rev. Lett.* **1996,** *77*, 3865-3868.

55. Blochl, P. E., Projector Augmented-Wave Method. *Phys. Rev. B Condens. Matter.* **1994,** *50*, 17953-17979.

56. Vanderbilt, D., Soft Self-Consistent Pseudopotentials in a Generalized Eigenvalue Formalism. *Phys. Rev. B Condens. Matter* **1990,** *41*, 7892-7895.

TOC graphic